

# Influence of debris flow solid fraction on rigid barrier impact

D. Song, C.W.W. Ng, C.E. Choi, G.G.D. Zhou, J.S.H. Kwan, and R.C.H. Koo

**Abstract:** The dynamics of debris flows are fundamentally governed by the interaction between the solid and fluid phases. However, current approaches used to estimate impact load treat debris flow as an equivalent fluid without considering solid–fluid interaction separately from other factors. In this study, a series of centrifuge tests was carried out to investigate the influence of interaction between solid and fluid phases on single-surge debris flow impact on a rigid barrier. The effect of solid–fluid interaction was studied by varying the solid fraction of the flows. A model rigid barrier was instrumented to capture induced bending moment and impact pressure. Test results demonstrate that the transition from a pile-up mechanism to a run-up mechanism is governed by the solid fraction and thus the grain contact stresses. The rigid barrier design for the impact with a pile-up mechanism is mainly dominated by the static load. Contrary to the hydrodynamic approach, which assumes that the frontal impact is the most critical, the frontal impact of a run-up mechanism contributes less than 25% of the total force impulse. The consideration of static loading leads to the development of a new impact model with a triangular distribution of the impact pressure.

*Key words:* debris flow, solid fraction, impact, rigid barrier, centrifuge modelling.

**Résumé :** La dynamique des flux de débris est fondamentalement régie par l'interaction entre les phases solides et liquides. Cependant, les approches actuelles utilisées pour estimer la charge d'impact traitent l'écoulement de débris comme un fluide équivalent sans tenir compte de l'interaction fluide solide séparément des autres facteurs. Dans cette étude, une série d'essais de centrifuge a été menée pour étudier l'influence de l'interaction entre les phases solide et liquide sur l'impact d'écoulement de débris cru unique sur une barrière rigide. L'effet de l'interaction fluide solide a été étudié en faisant varier la fraction solide des flux. Un modèle de barrière rigide a été instrumenté pour capturer le moment de flexion induit et la pression d'impact. Les résultats des essais montrent que le passage d'un mécanisme d'empilement (« pile-up mechanism ») à un mécanisme de montée (« run-up mechanism ») est régi par la fraction solide et donc les contraintes de contact de grains. La conception de barrière rigide pour l'impact à mécanisme d'empilement est principalement dominée par la charge statique. Contrairement à l'approche hydrodynamique qui suppose que le choc frontal est le plus critique, le choc frontal du mécanisme de montée contribue à moins de 25 % de la force totale d'impulsion. L'examen de la charge statique conduit à l'élaboration d'un nouveau modèle d'impact avec une distribution triangulaire de la pression d'impact. [Traduit par la Rédaction]

*Mots-clés :* flux de débris, fraction solide, impact, barrière rigide, modélisation par centrifuge.

## Introduction

Debris flows comprise mixtures of soil particles saturated in water (Hung et al. 2014; Takahashi 2014). Their complex flow dynamics is governed by the interaction between the solid and fluid phases. More specifically, the pore pressure regulates the Coulomb friction within and at the boundary of debris flows (Iverson and George 2014). The degree of interaction between the solid and fluid phases can partly be represented by the solid fraction of the flow. Flows with a larger solid fraction more readily dissipate flow energy from grain shearing (Choi et al. 2015b). Despite the availability of studies of solid–fluid interaction on debris flows mobility (Iverson 1997; McArdell et al. 2007; Johnson et al. 2012), a significant disparity of work has been carried out to understand the effect of solid–fluid interaction on impact behaviour.

The lack of understanding of the impact of debris flow is reflected in current engineering approaches used to estimate impact load. Existing methods predominantly rely on treating debris flow as an equivalent fluid. This means that solid–fluid interaction and the impact process are not considered explicitly. Such load models are convenient for engineering purposes, but fail to capture the key impact mechanisms such as run-up and pile-up (Choi et al. 2015a), and dead zone formation (Gray et al. 2003). The most commonly accepted model for estimating debris flow impact is the hydrodynamic model (Hung et al. 1984; Kwan 2012; Bugnion et al. 2012). This model is based on the conservation of momentum, assuming that the peak impact load  $F$  is generated upon frontal impact and is proportional to the dynamic pressure

$$(1) \quad F = \alpha \rho v^2 h w$$

Received 14 September 2016. Accepted 12 April 2017.

**D. Song.** Key Laboratory of Mountain Hazards and Earth Surface Process / Institute of Mountain Hazards and Environment, Chinese Academy of Sciences (CAS), Chengdu, China; formerly Department of Civil and Environmental Engineering, Hong Kong University of Science and Technology, Clear Water Bay, Kowloon, Hong Kong SAR.

**C.W.W. Ng\* and C.E. Choi.** Department of Civil and Environmental Engineering, Hong Kong University of Science and Technology, Clear Water Bay, Kowloon, Hong Kong SAR.

**G.G.D. Zhou.** Key Laboratory of Mountain Hazards and Earth Surface Process / Institute of Mountain Hazards and Environment, Chinese Academy of Sciences (CAS), Chengdu, China.

**J.S.H. Kwan and R.C.H. Koo.** Geotechnical Engineering Office, Civil Engineering and Development Department, Hong Kong SAR.

**Corresponding author:** C.E. Choi (email: [ceclarenc@ust.hk](mailto:ceclarenc@ust.hk)).

\*C.W.W. Ng currently serves as an Associate Editor; peer review and editorial decisions regarding this manuscript were handled by I. Moore.

Copyright remains with the author(s) or their institution(s). Permission for reuse (free in most cases) can be obtained from [RightsLink](https://www.rightslink.com).

where  $\alpha$  is the dynamic pressure coefficient,  $\rho$  is bulk density ( $\text{kg/m}^3$ ),  $v$  is frontal debris velocity ( $\text{m/s}$ ),  $h$  is flow depth ( $\text{m}$ ), and  $w$  is barrier width ( $\text{m}$ ). Equation (1) relies on one single compensating pressure coefficient to guarantee designs. The pressure coefficient  $\alpha$  is set somewhat arbitrarily although it is intended to be conservative to account for the current lack of understanding of the impact mechanisms and other factors of uncertainty.

The challenge in bearing further scientific insight on mechanisms of debris flow impact lies in the poor temporal predictability of natural flows and their scale-dependent behaviour. Geotechnical centrifuge modelling provides a means to overcome some of the scaling disparities. Bowman et al. (2010) carried out a series of centrifuge tests using saturated debris to investigate the debris mobility and entrainment. The tests to examine “modelling of models” (Schofield 1980) confirmed the feasibility of centrifuge for debris flow modelling. The test results were compared with the bulk parameters for the field scale debris flows. It is found that the centrifuge achieves closer similarity with prototype events compared with the 1g small scale modelling. Ng et al. (2017) carried out dry sand and viscous flows impacting rigid and flexible barriers in the centrifuge. The different mechanical response of the structures under impact was attributed to the nature of the two materials. More specifically, the dissipation of the debris kinetic energy was significantly enhanced via the stress-dependent friction and debris–barrier interaction. However, only simplified single-phase flows were examined and the effect of solid–fluid interaction on impact was not investigated. This makes it difficult to extrapolate results to understand the mechanisms of debris flow impact.

In this study, a series of centrifuge tests is carried out to investigate the effect of solid–fluid interaction of debris flow on the response of a rigid barrier. The interaction between the solid and fluid phases is achieved by varying the solid fraction of the flow. To ensure similitude with prototype flows, a two-level scaling approach is adopted. Furthermore, the load distribution on the rigid barrier is directly linked with the impact process of the two-phase flows.

## Two-level scaling

Scaling is a powerful tool to link geophysical processes at varying scales (i) to predict the outcome of one event from the results of another (Holsapple 1993); (ii) to guide the experimental design so that the model test outcome matches that of the prototype (Iverson 2015); (iii) to ascertain the key parameters of a certain phenomenon, even though the mechanism and material behaviour are not fully understood. In this study, a dimensionless group is used to design centrifuge model tests and the tests serve to bear new insight on debris flow impact.

A two-level scaling approach is adopted in this study. In the first level of scaling, the absolute stress states between the model and prototype must be correct and centrifuge modelling ensures this by elevating the centrifugal gravitational field  $N$  times. In the second level of scaling, the use of dimensionless groups (Iverson 1997, 2015) ensure that the relative ratios between selected stresses (i.e., stresses between the particles and fluid) in a model match those estimated in prototype. A two-level scaling approach of the absolute stress states and relative stresses in this study is a rigorous, systematic, and cost-effective alternative to large-scale modelling.

While centrifuge modelling provides well-controlled and well-instrumented testing conditions, simplifications are indeed necessary. These simplifications include adopting a uniform particle size and Newtonian fluid rheology. Another assumption required is selecting an appropriate prototype flow composition for the centrifuge model. The challenge lies in defining the size of fine particles that constitutes the fluid phase and thus influencing the viscosity. Based on theoretical considerations, Iverson (1997) as-

sumes that particle diameters less than 0.0625 mm should be classified as part of the fluid phase. By contrast, field monitoring results conclude particle diameters of up to 2 mm as the solid–fluid phase boundary (Fei et al. 1991). Furthermore, scaling between a centrifuge model and its prototype only ensures similarity of the known mechanisms, e.g., particle collision by the Savage number ( $N_s$ ) and pore fluid pressure dissipation by the inertial-diffusional time scale ratio. Mechanisms that are not well understood cannot be taken into account.

## Dimensionless group for debris flow characterization

The Froude number ( $Fr$ ) is widely adopted for characterizing the dynamic similarity in channelized granular flows (Chehata et al. 2003; Hauksson et al. 2007; Choi et al. 2014), hydraulics (Armanini et al. 2011; Lobovský et al. 2014), and geophysical flows (Hübl et al. 2009). The  $Fr$  macroscopically quantifies the ratio between the inertial and gravitational forces and is expressed as follows:

$$(2) \quad Fr = \frac{v}{\sqrt{g \cos \theta h}}$$

where  $g$  is gravitational acceleration ( $9.81 \text{ m/s}^2$ ) and  $\theta$  is the inclination of the channel. The rearrangement of eq. (2) leads to a much clearer physical representation of the comparison between inertial and gravitational forces

$$(3) \quad Fr^2 = \frac{v^2}{g \cos \theta h} = \frac{\rho v^2}{\rho g \cos \theta h}$$

The square of the Froude number  $Fr^2 > 1.0$  denotes supercritical flows, whereas  $Fr^2 < 1.0$  denotes subcritical flows. The Savage number characterizes the ratio of stress generated via instant grain collision stress and sustained grain contact shear stress and is expressed as follows:

$$(4) \quad N_s = \frac{\rho_s \dot{\gamma}^2 \delta^2}{(\rho_s - \rho_f) g h}$$

The Bagnold number represents the ratio of stress generated via grain collision stress and viscous stress and characterized as follows:

$$(5) \quad N_B = \left( \frac{v_s}{1 - v_s} \right) \frac{\rho_s \dot{\gamma} \delta^2}{\mu}$$

The inertial–diffusional time scale ratio quantifies the inertial to pore fluid pressure diffusional time scales and is represented as follows:

$$(6) \quad N_p = \frac{\sqrt{l/g}}{\mu h^2 / kE}$$

In equations (4)–(6),  $\rho_s$  is bulk density of solid grains ( $\text{kg/m}^3$ ),  $\dot{\gamma}$  is shear rate ( $1/s$ ),  $\delta$  is typical grain diameter ( $\text{m}$ ),  $\rho_f$  is the bulk density of pore fluid ( $\text{kg/m}^3$ ),  $l$  is flow length ( $\text{m}$ ),  $v_s$  is volumetric solid fraction,  $\mu$  is the dynamic viscosity of pore fluid ( $\text{Pa}\cdot\text{s}$ ),  $k$  is intrinsic permeability ( $\text{m}^2$ ) as a function of  $v_s$ , and  $E$  is bulk compressive stiffness of granular mixture ( $\text{Pa}$ ).

## Scaling principle of centrifuge modelling

Geomaterial behaviour is stress-state dependent (Ng 2014). In other words, if the stress conditions are greatly reduced, soil may undergo dilation rather than an expected prototype contractive response. Soil dilatancy or contraction has a significant effect on

**Table 1.** Relevant scaling laws.

Parameter	Dimension	Scaling law (model/prototype)
Gravity	$L/T^2$	$N$
Density	$M/L^3$	1
Length (depth and diameter)	$L$	$1/N$
Velocity	$L/T$	1
Inertial time	$T$	$1/N$
Shear strain rate	$1/T$	$N$
Stress	$M/(T^2L)$	1
Force	$ML/T^2$	$1/N^2$
Bending moment	$ML^2/T^2$	$1/N^3$

the pore pressures generated. The correct stress state between model and prototype conditions is essential to capture the proper response of solid phase and hence the solid–fluid interaction. An element in motion within the model develops a velocity scale factor of unity (Chikatamarla et al. 2006). Furthermore, based on the conservation of momentum (eq. (1)), the impact pressure also has a scale factor of unity since both the density and velocity have scale factors of unity. The scale factor for the impact force and bending moment reduces  $N^2$  and  $N^3$  times because of the reduced length scale, respectively (Ng et al. 2017). Scaling laws relevant to this study are summarized in Table 1.

## Centrifuge modelling of debris flow impact

### Model setup

The centrifuge tests in this study were carried out at the Geotechnical Centrifuge Facility at the Hong Kong University of Science and Technology. The 400g-t centrifuge has an arm radius of 4.2 m (Ng 2014). The tests were performed using a model container with plan dimensions of 1245 mm × 350 mm and a depth of 851 mm (Figs. 1a and 1b). The slope is inclined at 25°, with a channel width of 233 mm (5.2 m in prototype) and a length of 1000 mm (22.4 m in prototype). The Perspex of the model container and a partition are used to form a channelized slope. A storage container with a volume of 0.03 m<sup>3</sup> (model scale) was positioned over the slope. The distance between the bottom of the storage container and the top of the slope is about 500 mm (Fig. 1b). The storage container has a hinged door at the bottom. The door can be released in-flight using a hydraulic actuator. Once the container door is released, the debris will fall along the channel formed by the three side walls, rather than using a tube, on to the slope. The opening of the bottom door is 200 mm × 200 mm. The ratio between the opening size and particle diameter adopted in this study is 333, which is much larger than the criterion of jamming formation (6, Bowman et al. 2010). The two-phase suspension will consolidate in the centrifuge and needs to be released from outside the centrifuge (Bowman et al. 2010) or mixed continuously. To resolve this challenge, a customized helical ribbon mixer with a rated power of 2.2 kW (Fig. 1c) was installed inside the storage container to prevent solid–liquid segregation before the in-flight release of the two-phase material.

A 10 mm thick steel plate, 200 mm in height (4.5 m in prototype) and 233 mm (5.2 m in prototype) in width, was installed perpendicularly to the slope surface to model a cantilevered rigid barrier. The rigid barrier has a bending stiffness ( $EI$ , where  $E$  is Young's modulus and  $I$  is moment of inertia) of  $1.88 \times 10^8$  N·m<sup>2</sup> per metre run in prototype and is equivalent to a 0.9 m thick reinforced concrete wall.

The centrifuge tests were carried out under a nominal  $g$ -level of 25g at the base of centrifuge platform. The applied centrifugal gravity increases radially outward from the centrifuge axis (Schofield 1980; Bowman et al. 2010). At the mid-height of the rigid barrier, the actual  $g$ -level is 22.4g (Fig. 1b) and this value is adopted for the conversion of dimensions from model to proto-

type. From the bottom of storage container to the mid-height of rigid barrier, there is a difference in  $g$ -level of 3.2g (Fig. 1b), which corresponds to a 15% difference from the actual  $g$ -level. From the bottom to mid-height of the barrier, there is a difference in  $g$ -level of 0.7g, which corresponds to only 3% difference from the actual  $g$ -level.

### Instrumentation

Fifteen sets of semiconductor strain gauges (SGs) were mounted to measure the bending moment along the height of the model rigid barrier (Fig. 1d). Full Wheatstone bridge SGs were installed to compensate for temperature effect. The SGs have a gauge factor of 80 and are extremely sensitive. They are capable of measuring strains larger than  $1.5 \mu\epsilon$ . An epoxy coating was applied on the surface to protect the SGs.

Five dynamic load cells (range 0–100 N) with a diameter of 12 mm were embedded in the rigid barrier (Fig. 1d). The load cell surface was flush with the barrier surface. As the impact pressure changes most drastically during the debris frontal impact at the barrier base, the lower depths of the rigid barrier was more densely instrumented.

A high speed camera with a resolution of 1300 × 1600 pixels and sampling rate 640 frames per second was adopted (Fig. 1a). The influence of solid fraction on velocity attenuation and deposition processes behind the barrier was analysed using particle image velocimetry (PIV) analysis (White et al. 2003; Take 2015). Illumination was achieved by using two 1000 W light-emitting diode (LED) lights.

### Test programme

Prior to conducting impact tests, a series of calibration tests without rigid barrier was carried out at 22.4g. The dimensionless group (eqs. (3)–(6)) was calibrated at the location along the channel where the rigid barrier would be installed. Single-surge flow impact tests were then carried out. Typical solid fractions for saturated debris flows are larger than 0.4 (Iverson and George 2014), and saturated granular materials with a solid fraction larger than 0.8 rarely occur in a flowing state. Laboratory and field evidence indicate that the transition from flood to hyperconcentrated flow occurs when the solid fraction achieves a minimum of 3%–10% (Pierson 2005). To investigate the influence of solid fraction on the debris flow impact behaviour, the solid fraction is varied as 0.0, 0.2, 0.4, 0.5, and 0.58 to cover the range from flood, two-phase flow, and dry debris avalanches (Fig. 2 and Table 2). The solid fraction of the liquid saturated flows was limited to 0.5 in this study because of the limitation of the mixing system under elevated gravitational conditions in the centrifuge. Note that in test S, the interstitial fluid is air, but nevertheless can still be classified as a saturated flow. The interstitial fluid air has negligible resistance on granular movement (Iverson et al. 2004). The debris flows in this study is equivalent to a prototype volume of 170 m<sup>3</sup>.

### Grain diameter and pore fluid viscosity

The prototype flows in this study are simplified as ideal two-phase flows with pure viscous pore fluid and uniform solid grains. The fluid phase represents the water–fine grain mixture that flows freely in the modelled grains (solid phase). As aforementioned, the dimensionless numbers in centrifuge models should match those in prototype. According to the centrifuge scaling laws, the shear rate is scaled by a factor of  $N$ , because the velocity and linear dimensions scale by unity and  $1/N$ , respectively. To match the state of solid phase, the grain diameter  $\delta$  in Savage number  $N_s$  must also be scaled down  $N$  times. The reduction of the grain diameter in turn reduces the intrinsic permeability  $k$  in the inertial–diffusional time scale ratio  $N_p$ . Based on the Hagen–Poiseuille equation, with a reduced diameter of  $N$  times, the intrinsic permeability  $k$  reduces by  $N^2$  times. In addition, the empir-

Fig. 1. (a) Side view of model setup on centrifuge platform; (b) schematic of the model setup with g-level; (c) top view of the helical ribbon mixer system; (d) front face of rigid barrier and instrumentation. [Colour online.]

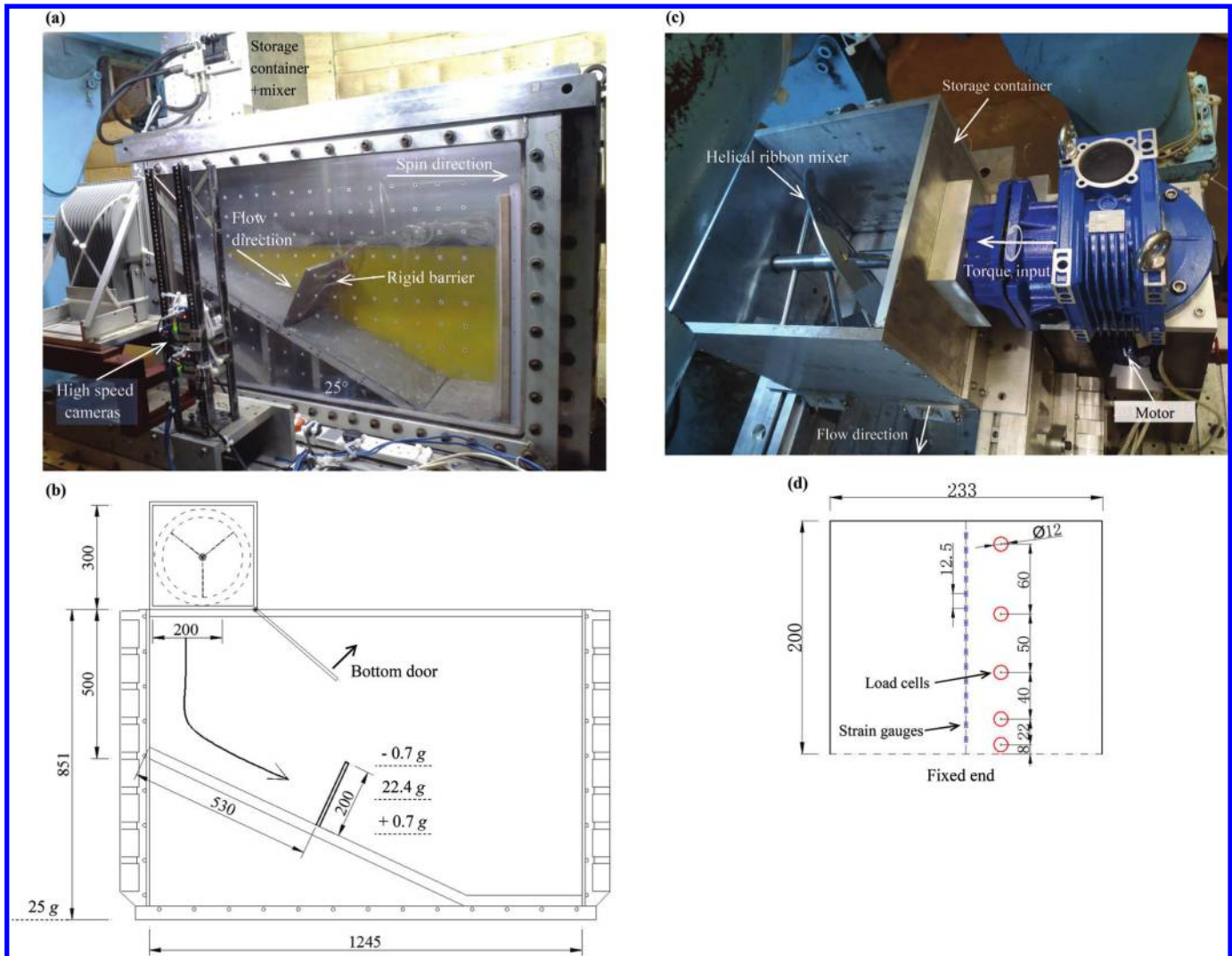


Fig. 2. Influence of solid fraction,  $v_s$ , on square of Froude number,  $Fr^2$ .

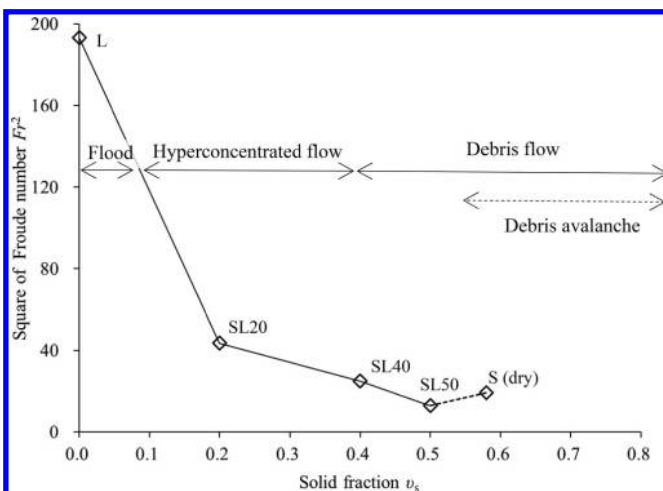


Table 2. Test programme and testing materials (all dimensions in model scale).

Material	Test ID	Solid fraction, $v_s$
Viscous liquid (0.022 Pa·s)	L	0.00
LB fraction C sand (0.6 mm) + viscous liquid (0.022 Pa·s)	SL20	0.20
	SL40	0.40
	SL50	0.50
LB fraction C sand (0.6 mm) + air (0.000 018 Pa·s)	S	0.58

Note: LB, Leighton Buzzard.

ical relationship between intrinsic permeability and solid fraction reported by Iverson and George (2014) is adopted in this study.

Two approaches are generally used to match the inertial and diffusional time scales in centrifuge modelling (Bowman et al. 2010). In the first approach, the prototype pore fluid viscosity  $\mu$  is replaced using a fluid with a viscosity  $N$  times higher to lengthen the times for diffusion by a factor of  $N^2$  and inertia by a factor of  $N$  in the model, resulting in the same overall time as observed under prototype conditions. In the second approach, the particle size  $\delta$  can be scaled by a factor of  $N^{0.5}$  while maintaining the same pore fluid viscosity,  $\mu$ . Following the Hagen–Poiseuille equation, the intrinsic

**Table 3.** Flow regime of the modelled flows.

Test ID	Solid fraction, $v_s$	Froude number, $Fr$ ; $Fr^2$	Savage number, $N_s$	Bagnold number, $N_B$	Inertial–diffusional time scale ratio, $N_P$
L	0.00	13.9; 193	—	0	0
SL20	0.20	6.6; 44	$1.5 \times 10^{-2}$	5	$6.5 \times 10^{1*}$
SL40	0.40	5.0; 25	$9.9 \times 10^{-3}$	11	$5.6 \times 10^{-1}$
SL50	0.50	3.6; 13	$4.5 \times 10^{-3}$	11	$3.4 \times 10^{-2}$
S	0.58	4.4; 19	$4.9 \times 10^{-3}$	$2.4 \times 10^4$	$5.5 \times 10^0$

\*With error in the permeability estimation.

sis permeability  $k$  is scaled down  $N$  times, so that both the inertial and diffusional time scales match at  $1/N$  of the prototype time scale. In this study, a third approach is proposed, specifically reducing the grain diameter  $\delta$  and the pore fluid viscosity  $\mu$ , both by  $N$  times. By adopting the third approach, the dimensionless group expressed in eqs. (3)–(6) becomes fully satisfied with prototype conditions. It is worthwhile to note that by adopting the third approach the diffusional time scale matches inertial time scale at a scale factor of  $1/N$ . This ensures that the loading rate on the structure is the same as prototype conditions.

Adopting uniform particles helps to simplify dimensional analysis (Iverson 1997). Leighton Buzzard (LB) fraction C silica sand is a commonly adopted testing sand in geotechnical engineering and comprises fairly uniform and rounded grains with diameters of about 0.6 mm (Choi et al. 2014). The specific gravity of the sand is 2.679 (Cavallaro et al. 2001) and its internal friction angle is  $31^\circ$ . The void ratio for LB sand is roughly measured as 0.6. A prototype fluid phase dynamic viscosity of  $0.5 \text{ Pa}\cdot\text{s}$  (Zhou and Ng 2010) was adopted in this study. This corresponds to a viscosity of  $0.022 \text{ Pa}\cdot\text{s}$  (22 times the viscosity of water) under room temperature  $20^\circ\text{C}$  in model scale. The viscous liquid adopted is a solution of water and carboxy methyl cellulose (CMC). The density of the viscous liquid closely resembles water ( $1000 \text{ kg/m}^3$ ). The two-phase flows in this study are mixed suspensions by external forces and they are all on the contractive side.

### Testing procedures

Once the model is prepared, the centrifuge was spun up to  $22.4g$ . Because the interaction time was scaled down to  $1/22.4$  of prototype conditions, a sampling rate of 20 kHz was selected to capture the kinematic and dynamic processes. After all the readings were stabilized, the storage container door was switched via the hydraulic actuator. The debris materials transitioned on to the slope and impacted the barrier. The bending moment, impact pressure, and high speed imagery were recorded. Finally, the centrifuge was spun down. The mixer remained functioning for the entire test process. It is acknowledged that the Coriolis effect influences the mobility of flowing sediments in a rotating system (Bryant et al. 2015; Bowman et al. 2012). However, the influence of the Coriolis acceleration diminishes rapidly once the flow impacts the barrier because the flow velocity rapidly attenuates through grain contact stresses and viscous shearing (Ashwood and Hungri 2016; Choi et al. 2015a; Koo et al. 2016).

## Results and interpretation

### Microscopic characterization

Both the Savage number  $N_s$  and Bagnold number  $N_B$  reflect the significance of collisional stresses of the granular materials over the grain contact friction and viscous shear stresses (Hsu et al. 2014) at the microscopic level. If the threshold reported by Savage and Hutter (1989) is adopted, for  $N_s < 0.1$ , the flows are in a grain contact regime rather than a collisional regime. Notwithstanding test S, the viscous effect dominates over grain collision according to the threshold reported by Bagnold (1954), specifically  $N_B < 40$  to 450. While viscous effects are more dominant than grain collisions, it does not necessarily mean that viscous effects strongly influence the flow behaviour. This is because grain collisions, in

fact, have a rather minor influence as indicated previously by the  $N_s$ . The flow regimes characterized using the aforementioned dimensionless group (eqs. (3)–(6)) from calibration tests of unobstructed channelized flow are summarized in Table 3.

### Influence of solid fraction on $Fr^2$

Test results show a sudden drop in  $Fr^2$  when comparing pure liquid flow (test L) to a flow with 0.2 solid fraction (test SL20, Fig. 2). The abrupt change in  $Fr^2$  reflects the significant effect of the solid fraction on debris mobility. As the solid fraction is increased from 0.2 (test SL20), the  $Fr^2$  progressively decreases and this implies a lower sensitivity to changes in solid fraction. The  $Fr$  of natural debris flows rarely exceeds 7.5 (Hübl et al. 2009). Field monitoring of the Illgraben catchment in Switzerland shows  $Fr$  estimations between 0.4 and 1.4 (McArdell et al. 2007). Based on experience in Hong Kong (Kwan et al. 2015), the debris flows in Hong Kong can be characterized using  $Fr$  of about 3 due to the abundant rainfall with steep natural terrain. Furthermore, experimental flows tend to develop relatively high  $Fr$  values, specifically 4 for the centrifuge modelling of dry sand and high viscosity liquid impact (Ng et al. 2017) and 7 for the USGS large-scale flume tests (Iverson 1997). The  $Fr$  with solid fractions equal or larger than 0.2 falls between 4 and 7 in this study. Note all the tests conducted in this study have the same potential heads. This indicates the strong effects of solid fraction and solid–fluid interaction in regulating the flow behaviour.

As the solid–fluid mixtures transition towards dry granular flow, an intermediate unsaturated flow state must exist. Debris flow fronts usually have higher permeability and are unsaturated as the process of particle-size reverse segregation transports coarse particles to the free surface and then to the front of a flow (Johnson et al. 2012). Unsaturated flows are characterized by enhanced internal shear strength due to the additional contact stress induced by the surface tension of water (Fredlund et al. 1978). Here a new dimensionless number  $N_{\text{suc}}$  is proposed to quantify the suction effect over frictional shearing and is expressed as follows:

$$(7) \quad N_{\text{suc}} = \frac{\psi_{\text{max}}}{\rho g h} = \frac{2T_s \cos \alpha_{\text{ws}}}{r_{\text{min}} \rho g h}$$

where  $\psi_{\text{max}}$  is the maximum matric suction (Pa) corresponding to the minimum pore radius  $r_{\text{min}}$  (m),  $T_s$  is the surface tension of water (N/m), and  $\alpha_{\text{ws}}$  is contact angle between water and soil. In this study, based on the definition of the maximum induced suction,  $\psi_{\text{max}}$  for the fraction C sand is about 200 Pa and significantly lower than the shear stresses generated in a 1 m deep flow. However, once fine particles like clays or silts are introduced into the flows, the effect of suction may no longer be trivial. In saturated flows, fines can migrate freely between large particles and the pore fluid viscosity is enhanced accordingly. For unsaturated granular flows, the fine contents may form clumps and adhere to the surface of large particles (Iverson et al. 2010). Matric suction, inversely proportional to the minimum void radius, acts as apparent cohesion. The apparent cohesion, over the flow process, is unlikely disturbed by large deformation because meniscus bridges

can be re-established. The existence of the suction effect can influence flow mobility and impact behaviour by enhancing the shear resistance of the flow. Owing to the suction effect, it remains conservative to use a straight (dashed) line to connect tests SL50 and S for the general relationship between solid fraction and  $Fr^2$  (Fig. 2).

### Impact patterns and mechanisms

PIV analyses are carried out for tests L, SL50 peak force and static state, and S (Figs. 3a, 3b, 3c, and 3d), respectively. The flow direction is from left to right. The initial interaction times in this study are reset to 1.0 s (0.045 s in model scale) as the flow front impacts the barrier. All dimensions are in prototype scale unless stated otherwise.

The pure liquid and two-phase flows in this study show a distinct run-up mechanism, while the dry sand flow exhibits a predominant pile-up mechanism (Choi et al. 2015a). The influence of solid fraction can be observed on the impact mechanism of the dead zone formation at the barrier base of tests SL50 and S. An increase in solid fraction results in more obvious and stagnant dead zones. Another influence of the solid fraction can be observed in the final deposition heights. Tests L, SL20, SL40, and SL50 have deposition heights that reach the crest of the barrier while test S only reaches about half of the barrier height. The two-phase flows remain well mixed until a static state was reached. The flowing debris as observed using the high-speed camera is uniform in colour along the flow depth, denoting a well-mixed state of the debris (Fig. 3b). After impact, the debris approaches a static state and a solid–fluid interface gradually appears (Fig. 3c), denoting the consolidation of the mixture.

It is postulated that there is a transition from a predominant run-up to pile-up mechanisms. To quantify such a transition, a sampling area of 1.5 by 1.5 times the frontal flow depth adjacent to the base of the barrier (Fig. 3a) is selected to obtain the mean velocity. The mean velocity attenuation with varying solid fractions is compared in Fig. 4. The prototype time and velocity are both normalized by a combination of flow length  $l$  and gravitational acceleration  $g$  (Iverson et al. 2004). Debris mixtures with larger solid fractions (tests SL40, SL50, and S) reach static conditions before a normalized time of  $t/\sqrt{l/g} = 1.0$ . This demonstrates the dominance of the effect of grain contact stresses. In contrast, debris mixtures with lower solid fractions (tests L and SL20) require a longer duration to reach static conditions and exhibit higher mean velocity fluctuations during the impact process. The test results further corroborate that viscous shearing is less effective at energy dissipation compared to grain shear stresses (Choi et al. 2015b; Ng et al. 2017).

### Rigid barrier dynamic response

The bending moment and impact pressure profiles along the barrier height were captured during the entire impact process. The bending moment profiles for tests SL20, SL50, and S are shown in Figs. 5a, 5b, and 5c, respectively. The time for peak bending moment to be generated by the low solid fraction impact is shorter, e.g., 1.2 s for test SL20 (Fig. 5a) versus 1.5 s for test SL50 (Fig. 5b). This is because the low-solid fraction flows are dominated by viscous stresses and are less efficient in converting the shear strain into shear stress. Consequently, higher mobility and loading rates develop upon impact. The bending moment profiles are nonlinear with their maximum values occurring at the barrier base. As run-up proceeds, the total force shifts upwards and the bending moment at the lower part of the barrier exhibits temporary linearity in test SL50 ( $t = 1.9$  and  $2.5$  s, Fig. 5b). This indicates that the distributed force at the time when the peak bending moment occurs, to a certain extent, acts like a point load on the rigid barrier. When the debris approaches a static condition, the moment once again becomes nonlinear.

The peak bending moment distribution for test S ( $t = 3.1$  s) is close to static conditions ( $t = 6.0$  s). Results indicate that for larger scale friction-dominated flows, as long as the impact mechanism is predominantly pile-up, the static forces on the structure should suffice for barrier design. Except for test S, a sharp peak bending moment observed in all tests, followed by a progressive decline in bending moment at static conditions coincides with the run-up mechanism. Whereas a gradual increase in bending moment time history observed in test S is consistent with the pile-up mechanism, the momentum is mainly resisted by the previously deposited debris (dead zone).

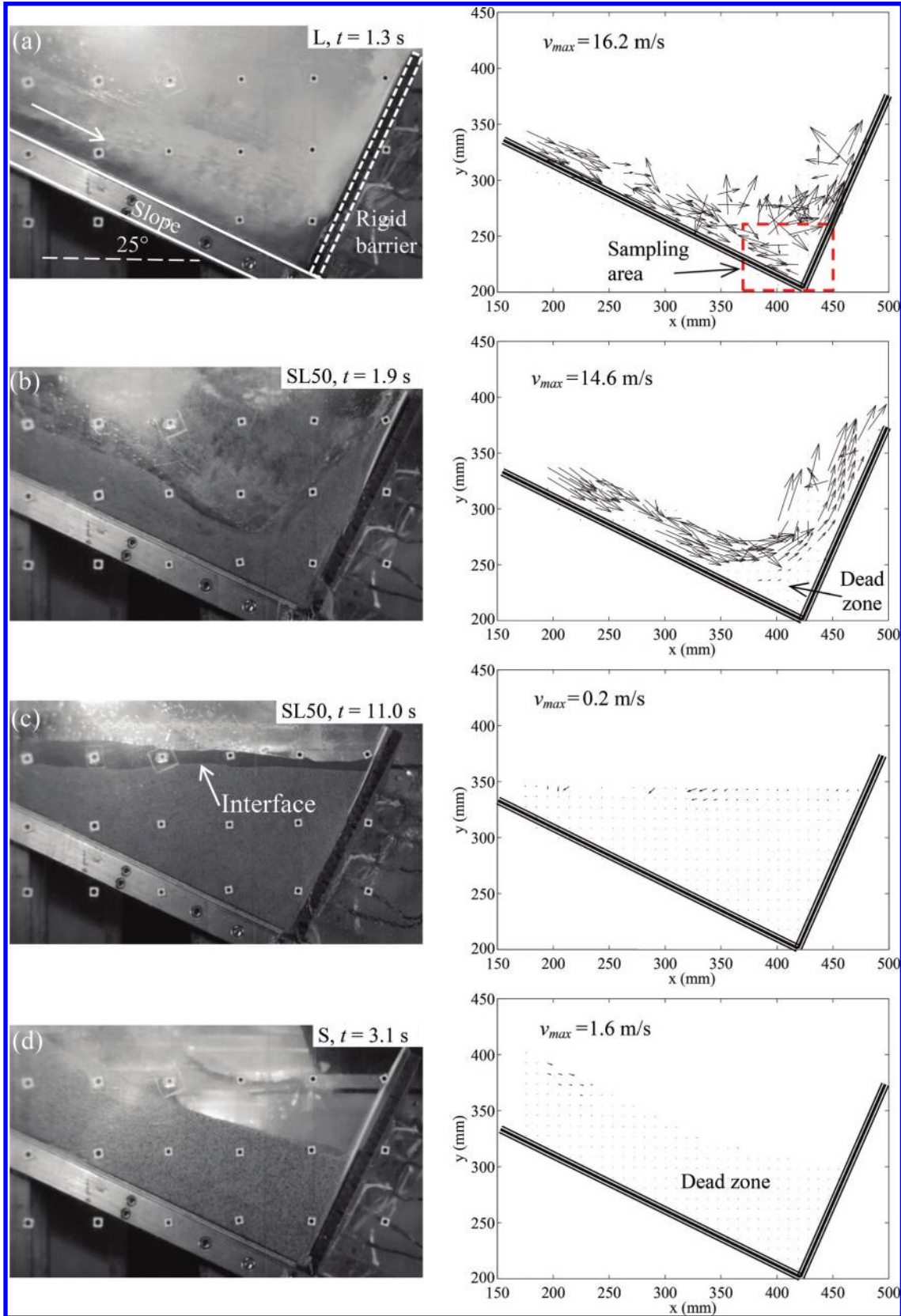
The impact peak pressure of test SL20 at the barrier base, load cell P1, occurs 0.3 s after the initial impact (Fig. 6a). Other load cells along the barrier capture response slightly later than P1. Compared to test SL20, test SL50 takes longer for the top load cell to detect an impact response (Fig. 6b), reflecting the high loading rate resulting from low solid fraction flow (L and SL20). After the initial impulse occurring between 1.0 and 1.2 s, P1 experiences a rapid drop of the peak pressure (1.2–1.8 s), followed by a much milder attenuation (1.8–6.0 s) and eventually static condition. The pressure time histories in test SL50 show less fluctuations compared to test SL20, which again reflects the efficiency of frictional energy dissipation. The impact pressure for test S also exhibits a sharp peak at the barrier base (Fig. 6c). However, the pressure is quickly suppressed by subsequent flow piling on top. Such a peak pressure usually cannot be detected using a single load cell to capture the total force on a rigid barrier (Moriguchi et al. 2009; Hübl et al. 2003). The inertial effect of the rigid barrier also functions as a filter to remove the short duration impulse loading on the barrier.

The evolution of pressure profiles at the occurrence of the peak pressure, peak force, and peak moment until static conditions are compared in Fig. 7. It can be observed that for two-phase flows (Figs. 7a and 7b), even during frontal impact, the loading exhibits distributions that increase almost linearly with depth. This observation is different from the rectangular pressure distributions reported by Cui et al. (2015). An increasing linear pressure distribution with depth (Fig. 7) corresponds to a cubic bending moment profile (Fig. 5). To cross-check measurements between strain gauges and load cells, the impact pressure of test SL50 at  $t = 2.5$  s is integrated twice to deduce the bending moment (Fig. 5b). The two measurements generally agree well with each other, thus corroborating the reliability of the measured impact responses. The pressure distribution of test S shows a first concave then convex shape. Such pressure distribution is controlled by the similar debris deposition shape during the gradual pile-up. The high correlation between the bending and free surface profiles supports that the loading process of test S is gravitational force dominated.

### Pressure impulse and contribution of frontal impact

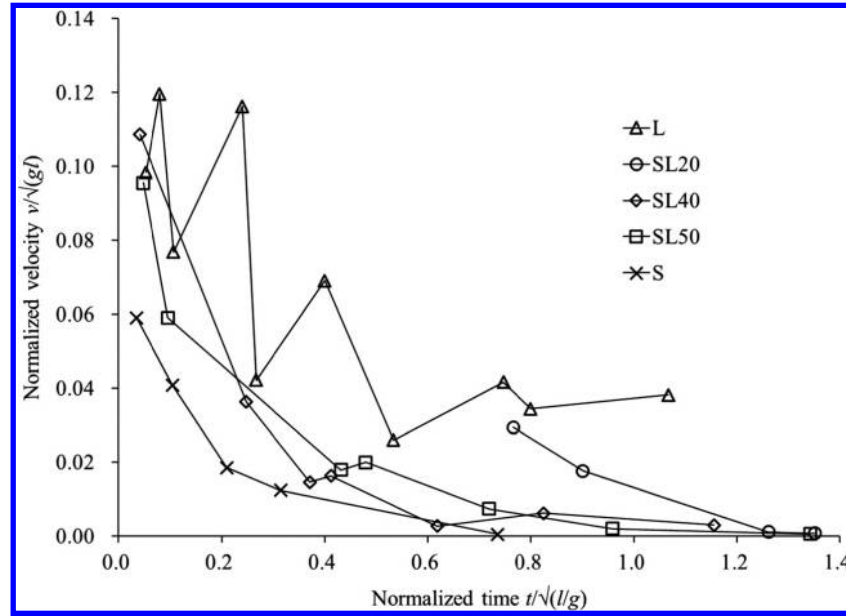
The dynamic pressure coefficient  $\alpha$  (eq. (1)) can be regarded as a normalized index between the measured and theoretical impact pressures. The peak impact pressure at the barrier base (load cell P1) is adopted to back-calculate the frontal  $\alpha$  value for each test. The results are summarized in Table 4. Based on the conservation of momentum, the theoretical frontal  $\alpha$  value is unity for flowing sediments without a static component acting on the barrier. Lobovský et al. (2014) conducted a total of 100 dam-break experiments using water to impact a rigid barrier and reported the median value of  $\alpha$  of about 1.25. However in this study, the results for tests L, SL20, and S are remarkably lower than unity. This is because some degree of compressibility exists in the flow. The compressibility can be observed through the entrainment of air bubbles (Fig. 3a), which may potentially lower the  $\alpha$  values. This is also a common phenomenon for the supercritical ( $Fr > 1$ ) hydraulic flume tests and natural floods. In contrast to liquid flows, the bulk compressibility of dry granular flow relies on particle rearrangement (contraction) under a high shear rate until

Fig. 3. Observed interaction kinematics for tests (a) L, peak force; (b) SL50, peak force; (c) SL50, static state; (d) S, peak force.



Can. Geotech. J. Downloaded from www.nrcresearchpress.com by "Chengdu Institute of Mountain Hazards and Environment, CAS" on 10/16/17  
For personal use only.

Fig. 4. Influence of solid fraction on mean velocity attenuation.



static conditions are reached (Forterre and Pouliquen 2008; Boyer et al. 2011). The two-phase mixtures (tests SL40 and SL50) resulted in  $\alpha$  values close to unity. It is postulated that the surface tension of the interstitial liquid prevents air from entering the dense granular flows, hence a lower degree of compression.

It is convenient to analyse the impact pressure from the perspective of pressure impulse because pressure impulse shows lower variability compared to that of peak impact pressure. The pressure impulse is defined as the integral of the pressure over the duration of the impact (Peregrine 2003; Lobovský et al. 2014). The integration of pressure can be simplified as a triangle to cover the peak impact area (see example of SL50 in Fig. 6b). In this study, the pressure of load cells P1 and P2 are adopted for the pressure impulse. Furthermore, the force impulse of the initial impact is the product of the pressure impulse and its relevant impact area.

Likewise, the total impact force on the whole barrier can be derived through summation of the pressure distribution along barrier height, and the total force impulse can also be derived by integration of force over the impact time. The total impact force-time history and a simplified triangular force impulse from test SL50 are shown in Fig. 8. Usually the rise time for the triangle is much shorter than the decay time, e.g., 0.9 s versus 5.0 s for test SL50.

The frontal impact is conventionally regarded as the most severe impact scenario by the current design guidelines. In this study, the contribution of frontal impact is quantified using the ratio between the frontal force impulse and the total impact impulse. The ratios for the pure liquid and two-phase flows impact are listed in Table 4. The ratio for test S is not included because the total force impulse is not clear for pile-up mechanism. Due to the limited interaction area of frontal impact, it can be observed that the frontal impact impulse only contributes less than 25% of the total impact force impulse. In other words, the frontal impact scenario is not the critical one for engineering design. A more rational impact scenario based on the run-up mechanism is discussed in the next section.

### Critical pressure profiles

The peak force and peak bending moment are two key parameters for designing retention structures. The pressure distributions at the occurrence of the peak force and bending moment at barrier base are further interpreted in this section (Fig. 9). The pressure value is normalized by  $\rho v^2$  and the corresponding run-up

height normalized by the flow depth  $h$ . The pressure profiles at peak force are generally triangular distributions with different maximum pressures occurring at the barrier base (Fig. 9a). As test SL50 has a solid fraction closest to natural debris flows, this pressure profile is adopted for interpretation. The triangular profile of interest can be represented by  $0.9\rho v^2$  and  $4.6h$ . The area of the triangle characterizes the total impact load. Test SL50 has a total impact force of about  $2.1\rho v^2 h w$ . According to the conservation of momentum, the theoretical impact force is  $\rho v^2 h w$  for pure fluid. The part higher than unit  $\rho v^2 h w$  denotes the static deposition load behind the barrier.

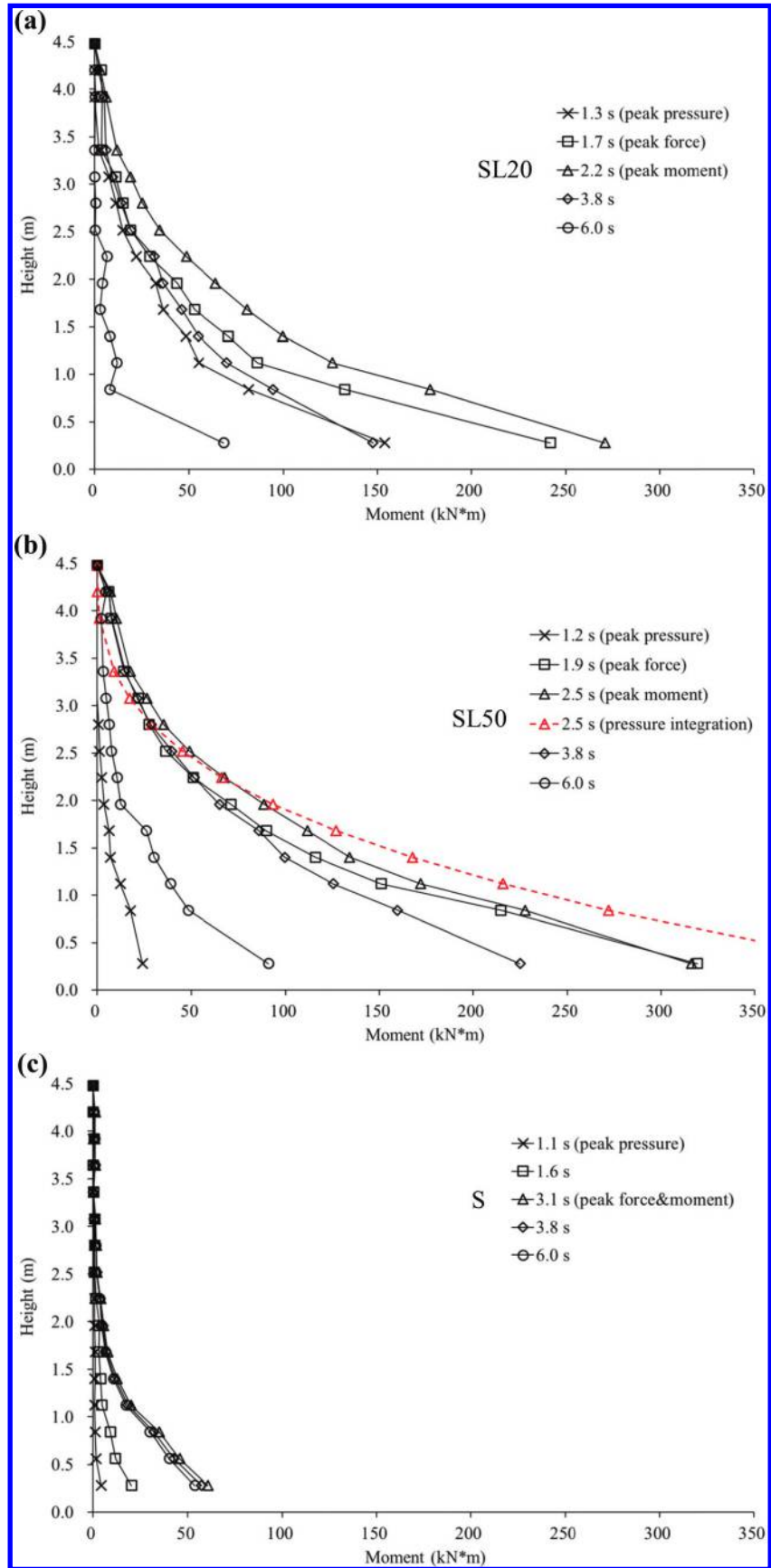
The profile of test SL50 at peak bending moment is triangular and can be represented by  $0.7\rho v^2$  and  $5.4h$  (at peak bending moment). The total force at peak bending moment time ( $1.9\rho v^2 h w$ ) is slightly lower than the peak force. As the run-up proceeds, the acting point to the barrier base ( $1.8h$ ) is higher than that of the peak force ( $1.5h$ ), implying a longer moment arm for the peak bending moment.

Apart from the static deposition, the pressure distribution patterns are also highly influenced by the structure type. Cui et al. (2015) reported the pressure distributions during the debris flowing around a rigid post, with a rectangular frontal pressure distribution and an inverse trapezoid (higher pressure at free surface) for the subsequent flows. The drag force acting around the obstacle near the free surface can be higher than the basal load induced by the static component, resulting in an inverse trapezoidal pressure distribution. Note that the rigid barrier in this study does not allow drag forces to develop around it. The purpose of a post-like structure is not to fully retain the debris, but rather to dissipate the kinetic energy. Hence, the run-up mechanism and triangular pressure distribution do not apply to individual obstacles.

Conventional load models (e.g., eq. (1)) assume the impact load acting on unit flow depth  $h$  is the most severe and the influence of other factors have been included using a dynamic pressure coefficient  $\alpha$  higher than 1.0. Such impact models cannot link the loading resulting from debris impact process. Based on the measured pressure distributions in this study (Figs. 9a and 9b), a triangular load model when the peak force and bending moment occur is proposed. The model considers run-up for barrier type structures (Fig. 9c)

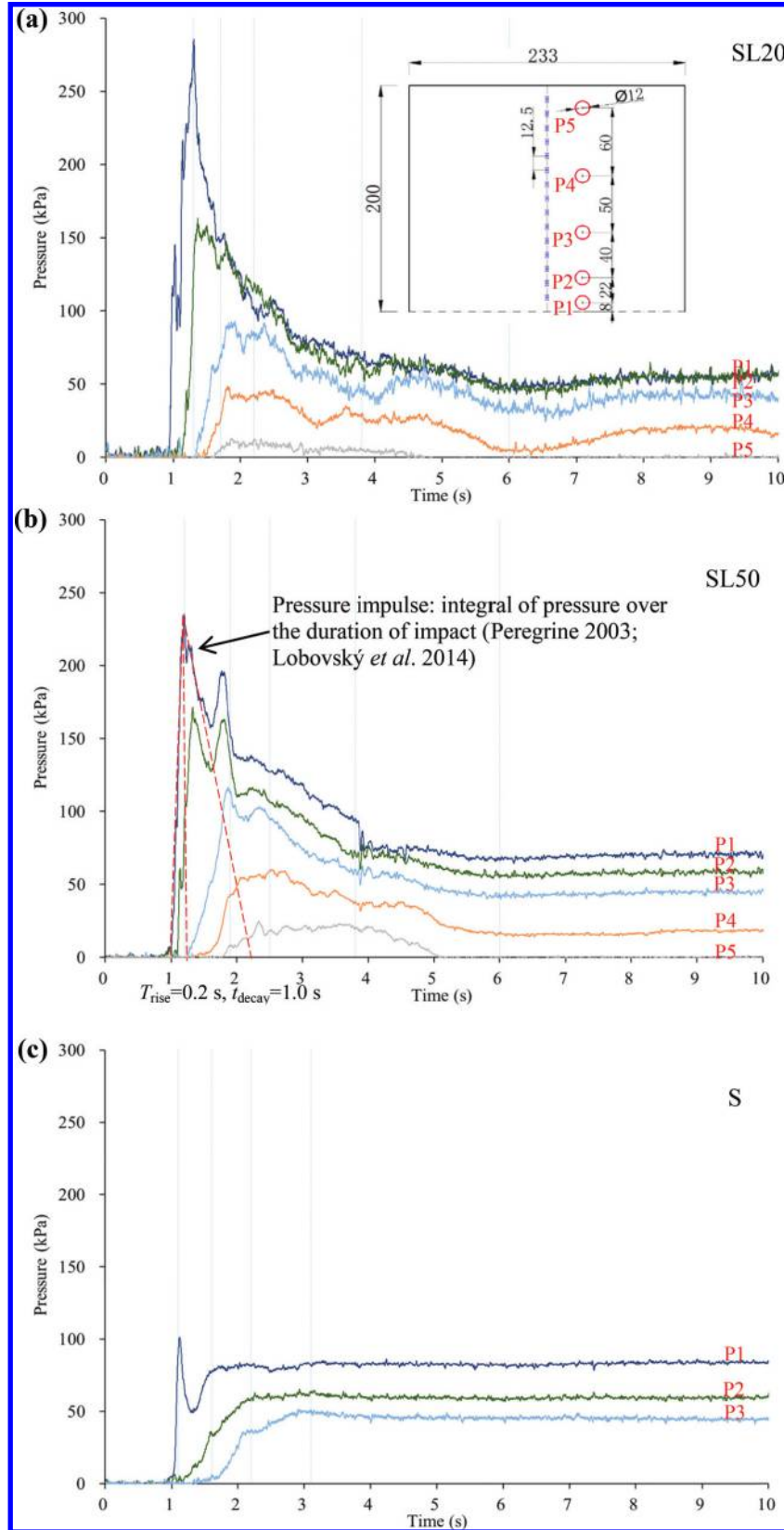
$$(8) \quad F = 0.5(\alpha' \rho v^2)(\beta h w)$$

Fig. 5. Bending moment profiles at critical time (i.e., peak pressure, force, and bending moment) for tests (a) SL20; (b) SL50; (c) S. [Colour online.]



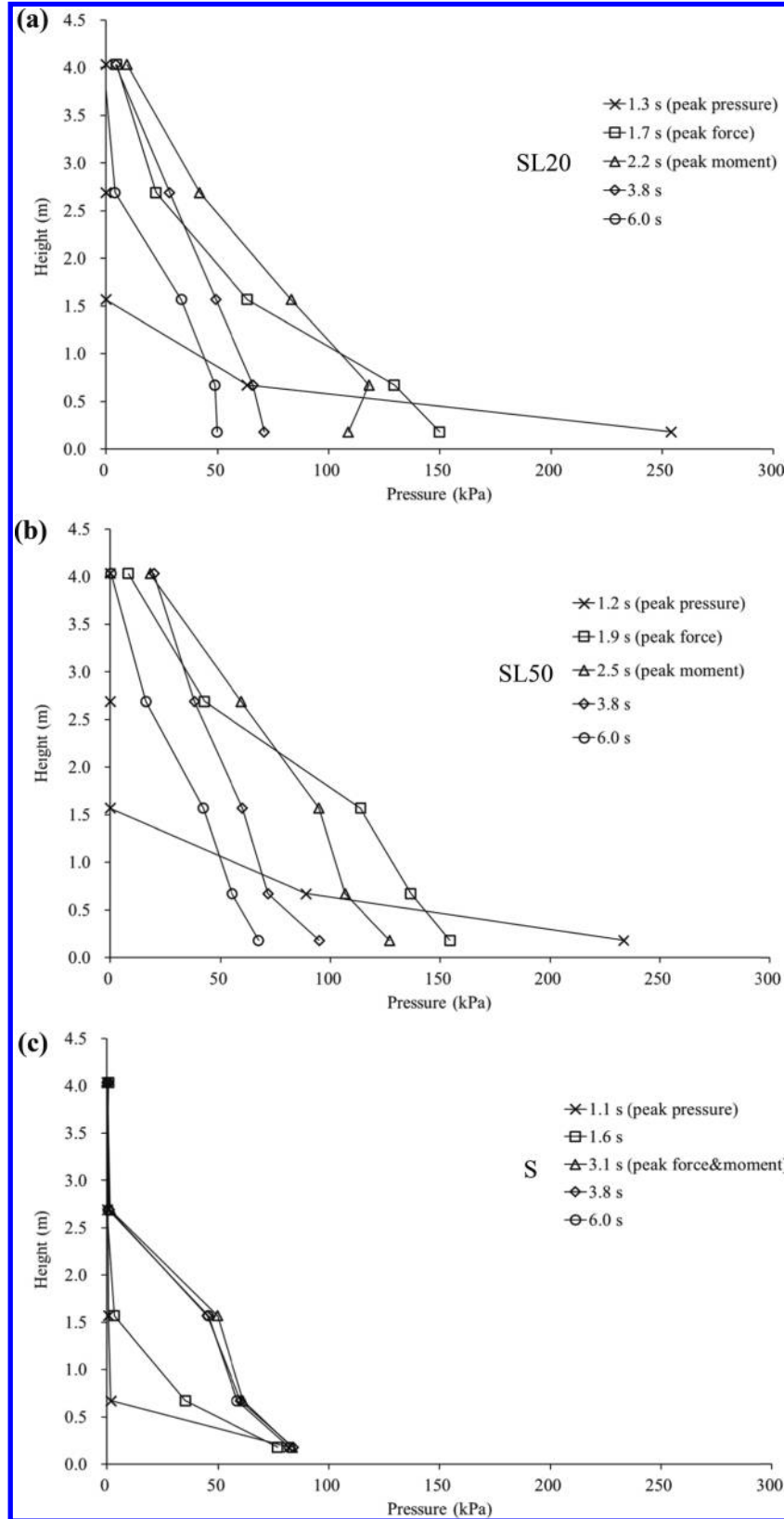
Can. Geotech. J. Downloaded from www.nrcresearchpress.com by "Chengdu Institute of Mountain Hazards and Environment, CAS" on 10/16/17  
For personal use only.

Fig. 6. Measured impact pressure time history for tests (a) SL20; (b) SL50 with pressure impulse of P1; (c) S. [Colour online.]



Can. Geotech. J. Downloaded from www.nrcresearchpress.com by "Chengdu Institute of Mountain Hazards and Environment, CAS" on 10/16/17  
For personal use only.

Fig. 7. Impact pressure profiles at critical time (i.e., peak pressure, force, and bending moment) for tests (a) SL20; (b) SL50; (c) S.



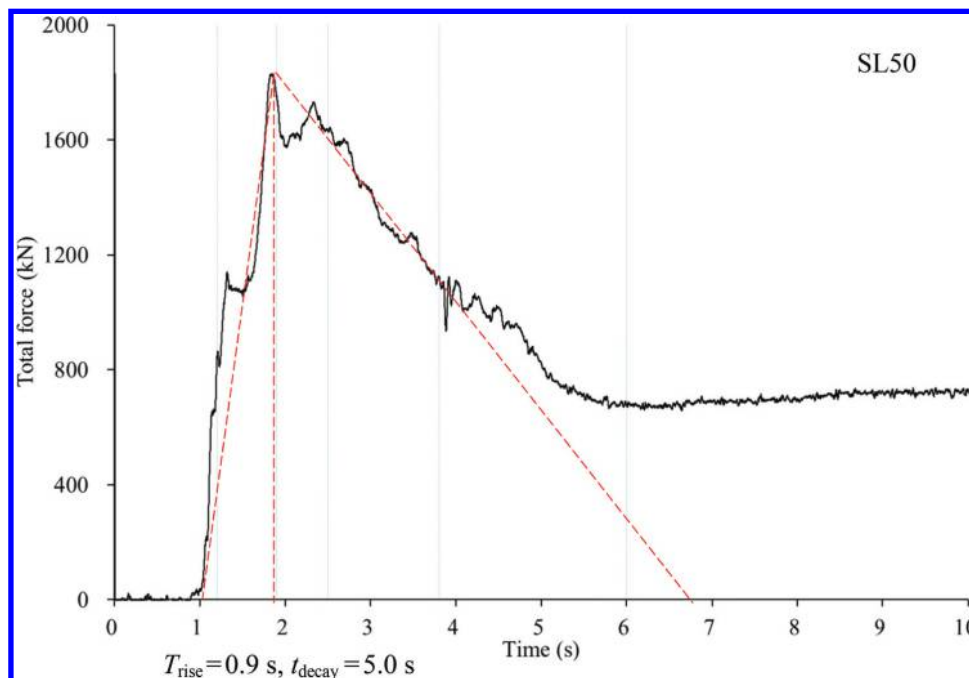
where  $\alpha'$  is the dynamic pressure coefficient considering the debris run-up and  $\beta$  is the run-up height normalized by the flow depth  $h$ . The total forces calculated based on eqs. (8) and (1) are the same, which means  $\alpha = 0.5\alpha' / \beta$ . However, eq. (8) can clearly depict

the distribution of the load based on physical test results. Consequently, the bending response can also be deduced. This ultimately allows the optimization of debris-resisting barriers. The pressure distributions generated during the peak force and peak

Can. Geotech. J. Downloaded from www.nrcresearchpress.com by "Chengdu Institute of Mountain Hazards and Environment, CAS" on 10/16/17 For personal use only.

**Table 4.** Dynamic pressure coefficients and contribution of frontal impact.

Test ID	Bulk density (kg/m <sup>3</sup> )	Frontal velocity (m/s)	Peak pressure (kPa)	Frontal dynamic pressure coefficient, $\alpha$	Remarks	Peak force dynamic pressure coefficient, $\alpha'$	Frontal force impulse (kN·s)	Total force impulse (kN·s)	Frontal/total force impulse ratio
L	1000	36.2	258	0.2	With bubbles, compressible	0.1	688	3470	0.20
SL20	1330	18.4	286	0.6	With bubbles, compressible	0.3	847	3324	0.25
SL40	1660	13.3	272	0.9	—	0.6	811	4651	0.17
SL50	1825	10.1	235	1.3	—	0.9	895	5399	0.17
S	1530	11.8	101	0.5	Particle rearrangement compressible	—	—	—	—

**Fig. 8.** Simplification of force impulse for test SL50. [Colour online.]

bending moment are triangular in shape. The maximum pressure of the triangular distribution is lower than the measured peak pressure during frontal impact. For tests exhibiting a predominantly run-up mechanism, the deduced  $\alpha'$  values are less than unity. This is because the momentum upon impact is transferred vertically along the barrier, rather than as concentrated loading at the base of barrier. Due to the enhanced effects of solid fraction on energy dissipation and debris mobility, the  $Fr$  decreases as the solid fraction increases (Fig. 2). Furthermore, debris impact comprises both the static component contributed by gravity and the dynamic component contributed by inertia, and the  $Fr$  is required to directly quantify the influence of the static or gravitational component (Armanini et al. 2011; Hübl et al. 2009). The  $\alpha'$  value increases as the  $Fr$  decreases (Table 4), attributing to the increasing contribution of static load and solid fraction.

Wendeler (2016) proposed a pressure-surge load model for the design of flexible barriers. This model considers the filling process of debris flow and assumes multiple surges of impact. Each surge contributes both static and dynamic components of the impact and after impact results in a static load on the barrier. Furthermore, the stiffness of a flexible barrier is not considered. Therefore, the model could also be applicable for rigid barriers (similar to Kwan 2012). However, the load model in this study only considers the pressure evolution for single-surge impact. The major difference between the models of this study and Wendeler (2016) is the implicit inclusion of static loading during the impact process.

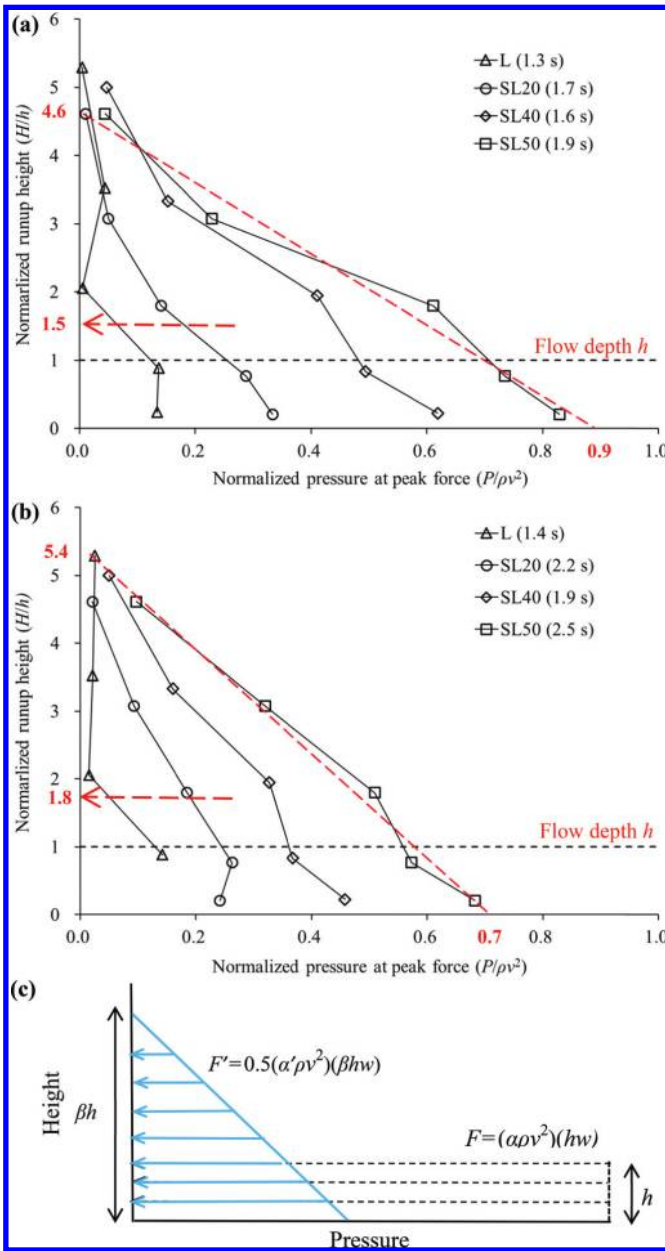
As a result of the static load, the dynamic pressure coefficient is a function of the  $Fr$ .

## Conclusions

A series of debris flow tests studying impact was carried out using a centrifuge. The stress state of the soil and solid-fluid stresses were appropriately scaled according to prototype debris flows. The solid fraction was varied to study the interaction between solid and liquid phases. Based on the captured impact kinematics and dynamic response of the barrier, the following conclusions may be drawn:

1. Pure liquid and two-phase flows develop a run-up mechanism; whereas dry granular flow exhibits a pile-up mechanism. The transition from run-up to pile-up mechanism is influenced by the increasing solid fraction. Larger solid fractions lead to increased grain contact stresses. Consequently, more stable dead zones form and less pressure fluctuations occur during the impact process.
2. The influence of solid fraction is also reflected by the loading rate on the rigid barrier. The close time between the occurrence of the peak pressure, peak force, and peak bending moment in the low solid fraction flows (tests L and SL20) denotes a higher loading rate and mobility; whereas the dry granular flow, test S, is characterized by the longest delay between the peak pressure and peak force. The coincidence between peak force and peak bending moment time indicates the domi-

**Fig. 9.** Impact pressure profiles at critical time (a) peak force; (b) peak moment; (c) simplified impact model. [Colour online.]



nance of the grain contract stresses and static load in the pile-up mechanism. This implies that the static force on the structure should suffice for barrier design with pile-up mechanism.

3. Tests exhibiting a run-up mechanism show that the contribution of the frontal impact impulse is lower than 25% of the total force impulse, regardless of the variation of the solid fraction. This implies that the frontal impact is not the most critical impact scenario for the debris flow developing a run-up mechanism and further corroborates the necessity to consider the impact mechanism when investigating debris-barrier interaction.
4. A new impact load model with consideration of the run-up mechanism is proposed for debris-structure interaction. The load model adopts a triangular load distribution with the maximum pressure occurring after the peak frontal impact pressure. A triangular load distribution highlights the static deposition contribution in the peak impact force and the efficiency of

frictional energy dissipation for dense two-phase flows. The proposed impact model enables the bending moment acting on a rigid barrier to be deduced.

**Acknowledgements**

The authors are grateful for financial support from research grant T22-603/15-N provided by the Research Grants Council of the Government of Hong Kong Special Administrative Region (SAR), China, and the HKUST Jockey Club Institute for Advanced Study. The authors acknowledge the support from the CAS Pioneer Hundred Talents Program and the National Natural Science Foundation of China (grant 11672318). This paper is supported by the Geotechnical Engineering Office and published with the permission of the Head of the Geotechnical Engineering Office and the Director of Civil Engineering and Development, the Government of the Hong Kong SAR.

**References**

Armanini, A., Larcher, M., and Odorizzi, M. 2011. Dynamic impact of a debris flow front against a vertical wall. *In Proceedings of the 5th International Conference on Debris-Flow Hazards Mitigation: Mechanics, Prediction and Assessment*, Padua, Italy. pp. 1041–1049.

Ashwood, W., and Hungr, O. 2016. Estimating total resisting force in flexible barrier impacted by a granular avalanche using physical and numerical modeling. *Canadian Geotechnical Journal*, **53**(10): 1700–1717. doi:10.1139/cgj-2015-0481.

Bagnold, R.A. 1954. Experiments on a gravity-free dispersion of large solid spheres in a Newtonian fluid under shear. *In Proceedings of the Royal Society A: Mathematical, Physical and Engineering Sciences*, **225**(1160): 49–63. doi:10.1098/rspa.1954.0186.

Bowman, E.T., Laue, J., Imre, B., and Springman, S.M. 2010. Experimental modelling of debris flow behaviour using a geotechnical centrifuge. *Canadian Geotechnical Journal*, **47**(7): 742–762. doi:10.1139/T09-141.

Bowman, E.T., Take, W.A., Rait, K.L., and Hann, C. 2012. Physical models of rock avalanche spreading behaviour with dynamic fragmentation. *Canadian Geotechnical Journal*, **49**(4): 460–476. doi:10.1139/t2012-007.

Boyer, F., Guazzelli, E., and Pouliquen, O. 2011. Unifying suspension and granular rheology. *Physical Review Letters*, **107**: 188301. doi:10.1103/PhysRevLett.107.188301. PMID:22107679.

Bryant, S., Take, W., Bowman, E.T., and Millen, M. 2015. Physical and numerical modelling of dry granular flows under Coriolis conditions. *Géotechnique*, **65**(3): 188–200. doi:10.1680/geot.13.P.208.

Bugnion, L., McArdell, B.W., Bartelt, P., and Wendeler, C. 2012. Measurements of hillslope debris flow impact pressure on obstacles. *Landslides*, **9**(2): 179–187. doi:10.1007/s10346-011-0294-4.

Cavallaro, A., Maugeri, M., and Mazzarella, R. 2001. Static and dynamic properties of Leighton Buzzard sand from laboratory tests. *In Proceedings of the Fourth International Conference on Recent Advances in Geotechnical Earthquake Engineering and Soil Dynamics*.

Chehata, D., Zenit, R., and Wassgren, C.R. 2003. Dense granular flow around an immersed cylinder. *Physics of Fluids*, **15**(6): 1622–1631. doi:10.1063/1.1571826.

Chikatamarla, R., Laue, J., and Springman, S.M. 2006. Centrifuge scaling laws for guided free fall events including rockfalls. *International Journal of Physical Modelling in Geotechnics*, **6**(2): 15–26. doi:10.1680/ijpmpg.2006.060202.

Choi, C.E., Ng, C.W.W., Song, D., Kwan, J.H.S., Shiu, H.Y.K., Ho, K.K.S., and Koo, R.C.H. 2014. Flume investigation of landslide debris-resisting baffles. *Canadian Geotechnical Journal*, **51**(5): 540–553. doi:10.1139/cgj-2013-0115.

Choi, C.E., Au-Yeung, S.C.H., Ng, C.W.W., and Song, D. 2015a. Flume investigation of landslide granular debris and water runup mechanisms. *Géotechnique Letters*, **5**: 28–32. doi:10.1680/geolett.14.00080.

Choi, C.E., Ng, C.W.W., Au-Yeung, S.C.H., and Goodwin, G.R. 2015b. Froude characteristics of both dense granular and water flows in flume modelling. *Landslides*, **12**(6): 1197–1206. doi:10.1007/s10346-015-0628-8.

Cui, P., Zeng, C., and Lei, Y. 2015. Experimental analysis on the impact force of viscous debris flow. *Earth Surface Processes and Landforms*, **40**(12): 1644–1655. doi:10.1002/esp.3744.

Fei, X.J., Kang, Z.C., and Wang, Y.Y. 1991. Effect on fine grain and debris flow slurry bodies on debris flow motion. *Journal of Mountain Research*, **9**(3): 143–152.

Forterre, Y., and Pouliquen, O. 2008. Flows of dense granular media. *Annual Review of Fluid Mechanics*, **40**: 1–24. doi:10.1146/annurev.fluid.40.111406.102142.

Fredlund, D.G., Morgenstern, N.R., and Widger, R.A. 1978. The shear strength of unsaturated soils. *Canadian Geotechnical Journal*, **15**(3): 313–321. doi:10.1139/t78-029.

Gray, J.M.N.T., Tai, Y.C., and Noelle, S. 2003. Shock waves, dead zones and particle-free regions in rapid granular free-surface flows. *Journal of Fluid Mechanics*, **491**: 161–181. doi:10.1017/S0022112003005317.

Hauksson, S., Pagliardi, M., Barbolini, M., and Jóhannesson, T. 2007. Laboratory measurements of impact forces of supercritical granular flow against mast-

Can. Geotech. J. Downloaded from www.nrcresearchpress.com by "Chengdu Institute of Mountain Hazards and Environment, CAS" on 10/16/17 For personal use only.

- like obstacles. *Cold Regions Science and Technology*, **49**(1): 54–63. doi:10.1016/j.coldregions.2007.01.007.
- Holsapple, K.A. 1993. The scaling of impact processes in planetary sciences. *Annual Review of Earth and Planetary Sciences*, **21**: 333–373. doi:10.1146/annurev.earth.21.1.333.
- Hsu, L., Dietrich, W.E., and Sklar, L.S. 2014. Mean and fluctuating basal forces generated by granular flows: laboratory observations in a large vertically rotating drum. *Journal of Geophysical Research: Earth Surface*, **119**(6): 1283–1309. doi:10.1002/2013JF003078.
- Hübl, J., Holzinger, G., and Wehrmann, H. 2003. Entwicklung von Grundlagen zur Dimensionierung kronenoffener Bauwerke für die Geschiebebewirtschaftung in Wildbächen: Klassifikation von Wildbachsperrern, WLS Report 50. Im Auftrag des BMLFUW VC 7a (unveröffentlicht). Wien: Institut für Alpine Naturgefahren, Universität für Bodenkultur.
- Hübl, J., Suda, J., Proske, D., Kaitna, R., and Scheidl, C. 2009. Debris flow impact estimation. In *Proceedings of the 11th International Symposium on Water Management and Hydraulic Engineering*, Ohrid, Macedonia. pp. 1–5.
- Hungr, O., Morgan, G.C., and Kellerhals, R. 1984. Quantitative analysis of debris torrent hazards for design of remedial measures. *Canadian Geotechnical Journal*, **21**(4): 663–677. doi:10.1139/t84-073.
- Hungr, O., Leroueil, S., and Picarelli, L. 2014. The Varnes classification of landslide types, an update. *Landslides*, **11**(2): 167–194. doi:10.1007/s10346-013-0436-y.
- Iverson, N.R., Mann, J.E., and Iverson, R.M. 2010. Effects of soil aggregates on debris-flow mobilization: results from ring-shear experiments. *Engineering Geology*, **114**(1–2): 84–92. doi:10.1016/j.enggeo.2010.04.006.
- Iverson, R.M. 1997. The physics of debris flows. *Reviews of Geophysics*, **35**(3): 245–296. doi:10.1029/97RG00426.
- Iverson, R.M. 2015. Scaling and design of landslide and debris-flow experiments. *Geomorphology*, **244**: 9–20. doi:10.1016/j.geomorph.2015.02.033.
- Iverson, R.M., and George, D.L. 2014. A depth-averaged debris-flow model that includes the effects of evolving dilatancy. I. Physical basis. *Proceedings of the Royal Society of London A: Mathematical, Physical and Engineering Sciences*, **470**(2170): 20130819. doi:10.1098/rspa.2013.0819.
- Iverson, R.M., Logan, M., and Denlinger, R.P. 2004. Granular avalanches across irregular three-dimensional terrain: 2. Experimental tests. *Journal of Geophysical Research: Earth Surface*, **109**(F1). doi:10.1029/2003JF000084.
- Johnson, C.G., Kokelaar, B.P., Iverson, R.M., Logan, M., LaHusen, R.G., and Gray, J.M.N.T. 2012. Grain-size segregation and levee formation in geophysical mass flows. *Journal of Geophysical Research*, **117**: F002185. doi:10.1029/2011JF002185.
- Koo, R.C.H., Kwan, J.S.H., Ng, C.W.W., Lam, C., Choi, C., Song, D., and Pun, W.K. 2016. Velocity attenuation of debris flows and a new momentum-based load model for rigid barriers. *Landslides*. doi:10.1007/s10346-016-0715-5.
- Kwan, J.S.H. 2012. Supplementary technical guidance on design of rigid debris-resisting barriers. GEO Report No. 270. Geotechnical Engineering Office, HKSAR Government.
- Kwan, J.S.H., Koo, R.C.H., and Ng, C.W.W. 2015. Landslide mobility analysis for design of multiple debris-resisting barriers. *Canadian Geotechnical Journal*, **52**(9): 1345–1359. doi:10.1139/cgj-2014-0152.
- Lobovský, L., Botia-Vera, E., Castellana, F., Mas-Soler, J., and Souto-Iglesias, A. 2014. Experimental investigation of dynamic pressure loads during dam break. *Journal of Fluids and Structures*, **48**: 407–434. doi:10.1016/j.jfluidstructs.2014.03.009.
- McArdell, B.W., Bartelt, P., and Kowalski, J. 2007. Field observations of basal forces and fluid pore pressure in a debris flow. *Geophysical Research Letters*, **34**: L07406. doi:10.1029/2006GL029183.
- Moriguchi, S., Borja, R.I., Yashima, A., and Sawada, K. 2009. Estimating the impact force generated by granular flow on a rigid obstruction. *Acta Geotechnica*, **4**(1): 57–71. doi:10.1007/s11440-009-0084-5.
- Ng, C.W.W. 2014. The state-of-the-art centrifuge modelling of geotechnical problems at HKUST. *Journal of Zhejiang University Science A*, **15**(1): 1–21. doi:10.1631/jzus.A1300217.
- Ng, C.W.W., Song, D., Choi, C.E., Liu, L.H.D., Kwan, J.S.H., Koo, R.C.H., and Pun, W.K. 2017. Impact mechanisms of granular and viscous flows on rigid and flexible barriers. *Canadian Geotechnical Journal*, **54**(2): 188–206. doi:10.1139/cgj-2016-0128.
- Peregrine, D.H. 2003. Water-wave impact on walls. *Annual Review of Fluid Mechanics*, **35**(1): 23–43. doi:10.1146/annurev.fluid.35.101101.161153.
- Pierson, T.C. 2005. Hyperconcentrated flow-transitional process between water flow and debris flow. In *Debris-flow hazards and related phenomena*. Springer Berlin Heidelberg. pp. 159–202.
- Savage, S.B., and Hutter, K. 1989. The motion of a finite mass of granular material down a rough incline. *Journal of Fluid Mechanics*, **199**: 177–215. doi:10.1017/S0022112089000340.
- Schofield, A.N. 1980. Cambridge geotechnical centrifuge operations. *Géotechnique*, **30**(3): 227–268. doi:10.1680/geot.1980.30.3.227.
- Takahashi, T. 2014. *Debris flow: mechanics, prediction and countermeasures*. CRC Press.
- Take, W.A. 2015. Thirty-Sixth Canadian Geotechnical Colloquium: Advances in visualization of geotechnical processes through digital image correlation. *Canadian Geotechnical Journal*, **52**(9): 1199–1220. doi:10.1139/cgj-2014-0080.
- Wendeler, C. 2016. Debris flow protection systems for mountain torrents - basic principles for planning and calculation of flexible barriers. WSL Berichte 44. [ISSN 2296-3456.]
- White, D.J., Take, W.A., and Bolton, M.D. 2003. Soil deformation measurement using particle image velocimetry (PIV) and photogrammetry. *Géotechnique*, **53**(7): 619–631. doi:10.1680/geot.2003.53.7.619.
- Zhou, G.G.D., and Ng, C.W.W. 2010. Dimensional analysis of natural debris flows. *Canadian Geotechnical Journal*, **47**(7): 719–729. doi:10.1139/T09-134.